Thermal Modeling of Resistance Spot Welding and Prediction of Weld Microstructure

M. SHEIKHI, M. VALAEE TALE, GH.R. USEFIFAR, and ARASH FATTAH-ALHOSSEINI

The microstructure of nuggets in resistance spot welding can be influenced by the many variables involved. This study aimed at examining such a relationship and, consequently, put forward an analytical model to predict the thermal history and microstructure of the nugget zone. Accordingly, a number of numerical simulations and experiments were conducted and the accuracy of the model was assessed. The results of this assessment revealed that the proposed analytical model could accurately predict the cooling rate in the nugget and heat-affected zones. Moreover, both analytical and numerical models confirmed that sheet thickness and electrode-sheet interface temperature were the most important factors influencing the cooling rate at temperatures lower than about $T_l/2$. Decomposition of austenite is one of the most important transformations in steels occurring over this temperature range. Therefore, an easy-to-use map was designed against these parameters to predict the weld microstructure.

I. INTRODUCTION

RESISTANCE spot welding (RSW) is one of the most prevalent welding processes in sheet metal joining and the automotive industry. The weld properties are affected by many parameters involved in the RSW process. Thus, many investigations have so far been carried out to examine these relationships.[1–4] It has been demonstrated that weld strength, impact resistance, and formability of the produced weld by the RSW process mainly depend on the nugget dimensions, *i.e.*, diameter and penetration.[1,2] The mechanical properties of the produced joint also depend on the weld integrity and its microstructure.[1,2,5]

It seems important to determine how operating conditions influence the preceding factors. Numerical simulation is the best alternative method to understand the RSW mechanism, helping to determine the parameters of the process so that the appropriate weld can be produced. Despite considerable investigations on numerical simulations of RSW,[6–13] the development of analytical models still requires close attention focused on this process. An analytical approach can help researchers gain a better understanding of the RSW

process by finding the relations between the weld properties and the governing process parameters.[4,14] Gould *et al.* proposed a simple one-dimensional analytical model to predict the cooling rate of the RSW process.[14] Based on this model, the cooling rate ($\dot{T}$) at any temperature (T) could be obtained as follows:

$$\dot{T} = \left(\frac{\alpha\pi^2}{4h^2}\right)\left(\frac{T}{T_{\max}}\right)\left[\frac{T}{1 + \left(\frac{2}{\pi}\right)\left(\frac{k_E}{k_S}\right)\left(\frac{h}{h_E}\right)\cos\left(\frac{\pi}{2h}x\right)} - T_{\max}\right],$$

[1]

where $T_{\max}$ is the nugget peak temperature; h is the sheet thickness; k_E and k_S are the thermal conductivities of the electrode and sheet, respectively; and h_E is the distance between the water-cooled surface of the electrode and the contacting electrode surface. Determining $T_{\max}$ and ignoring the nugget dimensions are the most important problems associated with this model.

The purpose of this survey was to put forward a more accurate thermal model to be used during the cooling step to obtain a deeper understanding of the systematic relation between the welding variables, the cooling rate, and the resultant weld microstructure. To evaluate the analytical model, a quarter of the symmetric model as the solution domain was analyzed by the finite element method. Due to the symmetry of the process, only a quarter of the welding zone was modeled and subsequently analyzed using the finite element method. To assess the calculations, the effect of the welding current in the spot resistance welding of carbon steel sheets was experimentally investigated.

M. SHEIKHI, M. VALAEE TALE, and ARASH FATTAH-ALHOSSEINI are with the Department of Materials Engineering, Bu-Ali Sina University, Hamedan 65178-38695, Iran. Contact e-mail: sheikhi.mohsen@basu.ac.ir GH.R. USEFIFAR is with the SAIPA Corporation, Tehran, Iran.
Manuscript submitted February 8, 2017.
Article published online September 12, 2017.

Table I. Chemical Composition of Used Steel Sheet (Weight Percent)					
Chemical Composition					
C	Mn	Si	Ni	Cr	Fe
0.06	0.23	0.025	0.045	0.01	balance

Table II. Welding Operating Parameters Used in the Experiments				
Squeeze Time (Cycle)	Welding Time (Cycle)	Holding Time (Cycle)	Welding Current (kA)	Electrode Force (kN)
10	10	10	8, 10, 12	50

II. EXPERIMENTAL PROCEDURE

In this investigation, low-carbon steel sheets (thickness = 0.7 mm and radius = 3 cm) were used for welding. The chemical composition of the used material is listed in Table I.

The spot welding process was carried out by a single-phase machine, *i.e.*, 55 kVA and 50 Hz AC. A pair of water-cooled cone-shaped flat Cu-Cr alloy electrodes (6.0-mm face diameter) was used for welding. Welding conditions are summarized in Table II. It should be mentioned that all welding parameters were kept constant during the welding process except the welding current. In this research, the root-mean-square value of the welding current was reported as the welding current.

To study the weld microstructures using optical microscopy, the weld samples were sectioned across the nugget. They were subsequently ground, polished, and etched by means of 2 pct Nital reagent. Vickers microhardness of the specimens used was tested at 100-g loading condition.

III. MODELING AND SIMULATION

Based on the studies that have so far been done regarding RSW,[4,14] it seems reasonable to presume that the bulk of heat transfer takes place in this process by the conduction through the water-cooled electrodes, along the sheet thicknesses (z direction in Figure 1). Accordingly, a one-dimensional heat-transfer governing equation was considered so as to develop an analytical model during the cooling step:

$$\frac{\partial T}{\partial t} = \alpha \frac{\partial^2 T}{\partial z^2}. \qquad [2]$$

In this equation, t is time after cutting off the current and α represents the heat diffusivity equal to $k/\rho c_p$, where k is the thermal conductivity, ρ is the density, and c_p is the specific heat. Concerning boundary conditions, it was assumed that the electrode-sheet contacts had ideal conditions and the thermal resistance was ignored.

Therefore, the temperatures of the outer sheet surface (T_S) and the electrode surface were kept equal during the cooling step; that is,
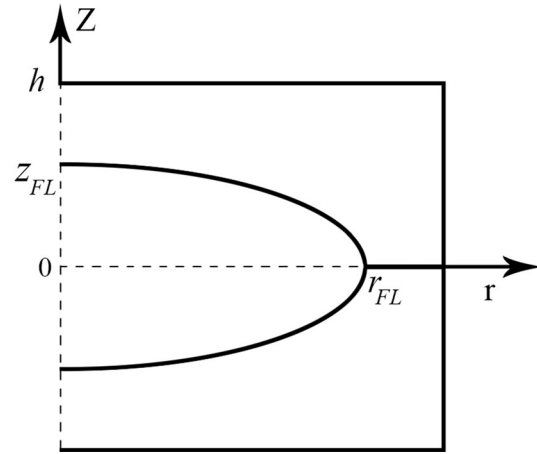

Fig. 1—Schematic illustration of the nugget zone and corresponding dimensions.

$$T(z = h, t) = T_S, \qquad [3]$$

where h is the sheet thickness at the welding zone. The analytical solution of this equation can be done by the separation of the variable technique. In this method, the temperature function is only expressed as a product of a function of position [$F(z)$] and a function of time. Accordingly, the initial condition can be stated as follows:

$$T(z, t = 0) = F(z), \qquad [4]$$

where $F(z)$ is the temperature distribution function over sheet thickness (along the z direction) at the moment of the current termination. Results of the previous investigations[6–10] revealed that the temperature profile along the sheet thickness at $t = 0$ was close to trapezoid. Thus, the following equation was considered for the positional function:

$$F(z) = \frac{8(T_{max} - T_S)}{\pi^2 \times (1 - \beta)} \sum_{k=1}^{n} \frac{1}{(2k - 1)^2}$$
$$\times \cos\left[\frac{(2k - 1)\pi}{2}\beta\right] \cos\left[\frac{(2k - 1)\pi}{2 \times h}z\right] + T_S, \qquad [5]$$

where n identifies the number of series terms and β is the fraction of sheet thickness ($0 < \beta < 1$) melted by

the welding and can be obtained through the following equation:

$$\beta = \left(\frac{z_{FL}}{h}\right), \qquad [6]$$

where z_{FL} is the distance between the nugget boundary and the faying surface in the z direction (Figure 1).

With respect to the proposed equation for the initial temperature profile, the solution of Eq. [2], using the separation of the variable technique, yields

$$T = \frac{8(T_{max} - T_S)}{\pi^2 \times (1 - \beta)} \sum_{k=1}^{n} \frac{1}{(2k-1)^2} \cos\left[\frac{(2k-1)\pi}{2}\beta\right]$$
$$\times \cos\left[\frac{(2k-1)\pi}{2 \times h}z\right] \exp\left[-\frac{\alpha(2k-1)^2\pi^2}{4h^2}t\right] + T_S.$$
$$[7]$$

It should be mentioned that, due to the great temperature dependency of the specific heat, thermal conductivity, and mass density, the average values of these parameters, between the solidus and room temperatures, were used to calculate the thermal diffusivity; this assumption yields $\alpha \cong 2.7 \times 10^{-6}$. Moreover, the latent heat of solidification, solid-state phase transformation, and recrystallization were all neglected in these computations. These simplifications can be regarded as a source of differences observed in the obtained results, especially in the temperature range of the phase transformations.

The temperature of the electrode-sheet interface (T_S) experienced some variations during welding. In order to calculate these variations during the cooling step, the heat flux boundary condition, with the assumption of the linear temperature distribution within the electrode thickness, at $z = h$ can be defined as follows:

$$k_E \frac{T_S - T_w}{Z_E} = k_s \frac{\partial T}{\partial z}, \qquad [8]$$

where T_w is water temperature, k_E is electrode thermal conductivity, and Z_E is electrode face thickness (10 mm). So, T_S can be obtained by combining Eqs. [7] and [8] as follows:

$$T_S = T_{max} + T_w$$
$$- \frac{T_{max}}{1 + \frac{4k_s}{\pi \times (1-\beta) \times h}\frac{Z_E}{k_E}\sum_{k=1}^{n}\frac{(-1)^{k-1}}{(2k-1)}\cos\left(\frac{(2k-1)\pi}{2}\beta\right)\exp\left(-\frac{\alpha(2k-1)^2\pi^2}{4h^2}t\right)}.$$
$$[9]$$

In order to obtain the initial temperature profile along the sheet thickness in the cooling step, *i.e.*, at the moment of current termination, and to evaluate the proposed analytical model, the welding process was simulated by the finite element package *ABAQUS*. For reasons of symmetry, only a quarter of the welding zone was modeled by means of a three-dimensional model on which appropriate initial and boundary conditions were applied. Figure 2 illustrates the geometry of the simulation domain along with the boundary conditions.
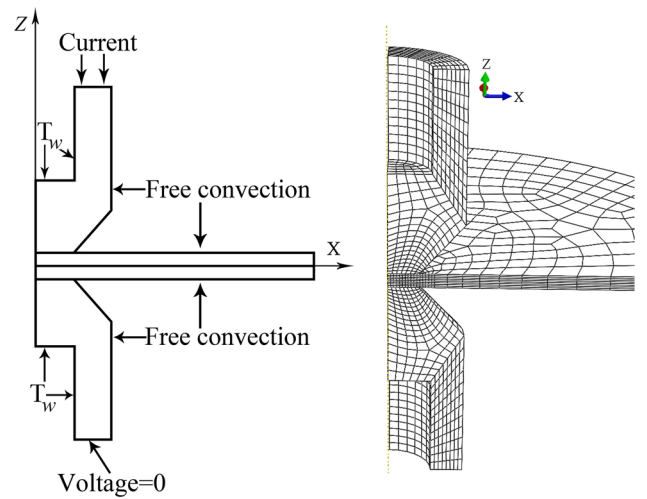

Fig. 2—Geometrical illustration of the calculation domain along with the boundary conditions and mesh used in the simulations.

Initial temperatures of the sheets and electrodes were set equal to the room temperature. Welding current was applied by the surface current load with uniform distribution on the top surface of the upper electrode. Temperature dependency of the material and contact properties were taken into account in the numerical model, as shown in Figure 3. For both E/S and S/S contacts, corresponding electrical resistances[13,15] were defined in the interaction property in the coupled thermal–electrical analysis.

In the simulation, heat loss due to the free convection on the outer surfaces of the sheets and electrodes was also taken into account. It was supposed that the temperature of water-cooled electrode surfaces did not change and during the welding process it was kept constant, *i.e.*, equal to the water temperature. It should be said that weld pool convection was ignored in these calculations.

IV. RESULTS

The hardness profile of the created nugget, using 12-kA welding current, is plotted in Figure 4(a). It is seen that the nugget zone has the highest hardness compared with the heat-affected zone (HAZ) and the base metal. It should be noted that hardness profiles in other welding conditions also followed the same trend. The mean hardness of the nugget zone and the lateral HAZ for all samples are summarized in Figure 4(b).

Contrary to our expectations, it was seen that the average hardness of the nugget and HAZ increased as the welding current increased from 8 kA to 10 and 12 kA.

Process parameters were applied to the numerical model to calculate the nugget dimensions and thermal histories under different welding conditions. Figure 5 shows the computed thermal histories at the faying surface and the electrode-sheet interface for the weld sample created using 12-kA welding current.
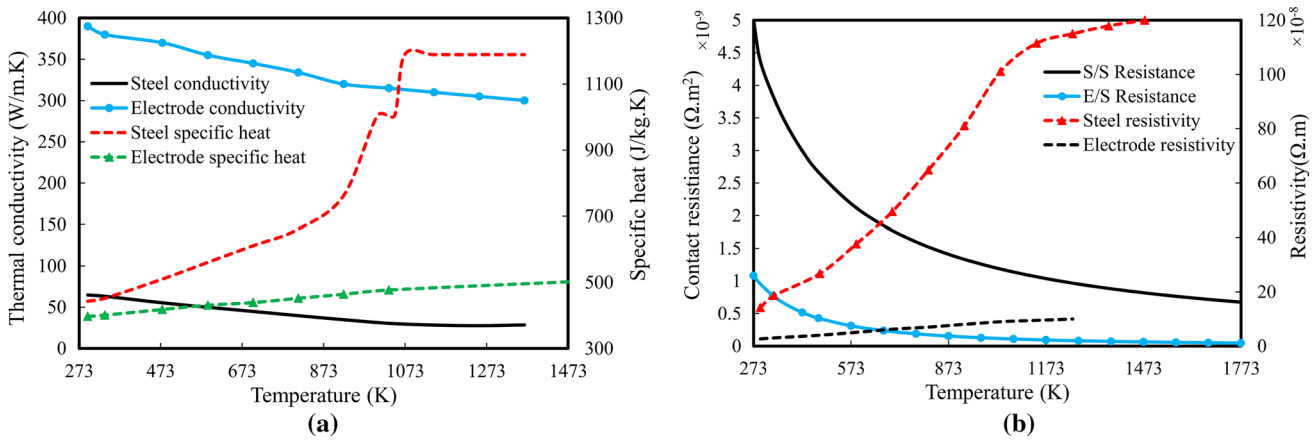
Fig. 3—Temperature-dependent properties used in the simulations: (a) thermal conductivity and specific heat and (b) electrical resistivity and electrical contact resistance.
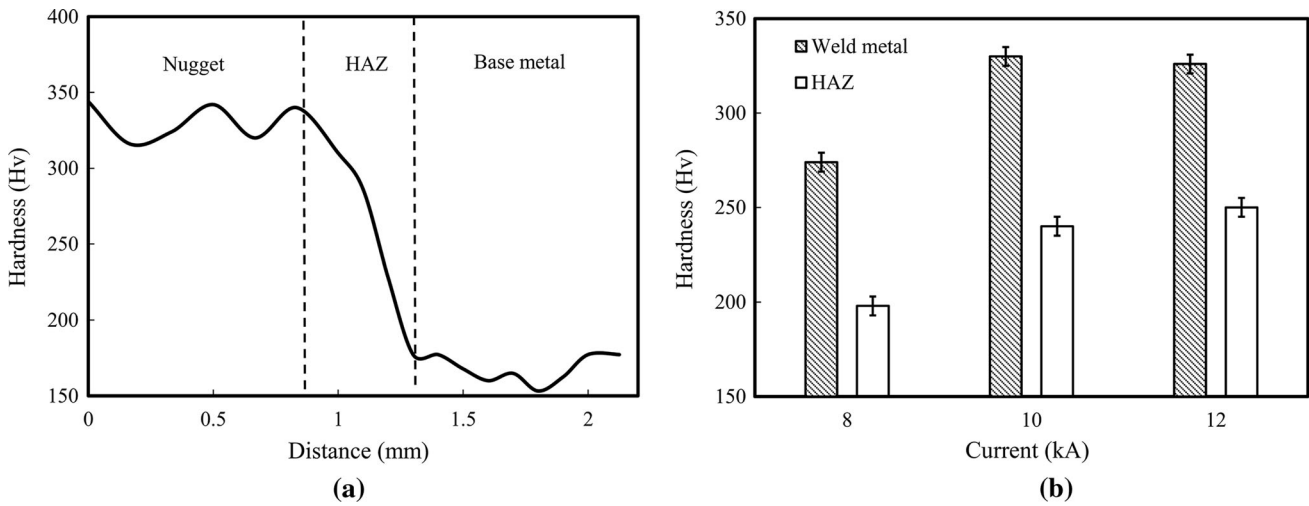

Fig. 4—Experimentally measured hardness: (a) hardness profile along the r direction of the weld zone created by 12 kA and (b) average values of the microhardness of the nugget and HAZ corresponding to various welding currents.
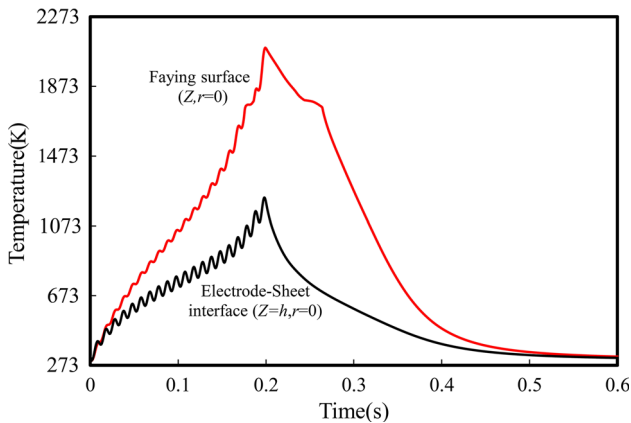

Fig. 5—Thermal histories at the faying surface and sheet-electrode interface for the weld created by 12-kA welding current.
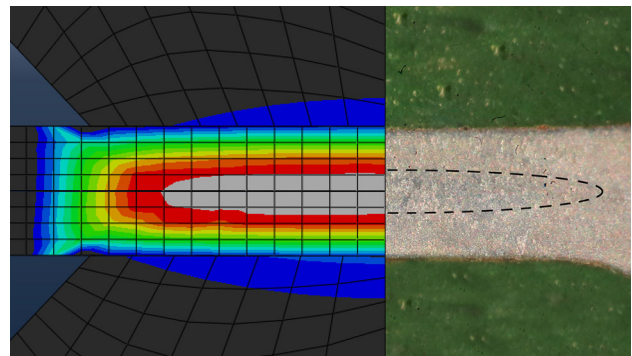

Fig. 6—Comparison of the experimental and calculated nugget shape for the welded sample using 8-kA welding current.

In the simulations, the nugget zone was considered as the region experiencing peak temperatures above 1793 K (1520 °C). Comparing the real nugget shape and the numerically predicted one revealed that the numerical model could estimate the nugget dimensions with errors lower than 15 pct (Figure 6).

Table III. Effect of n on the Accuracy of Predicted T_{max} at Different β Values

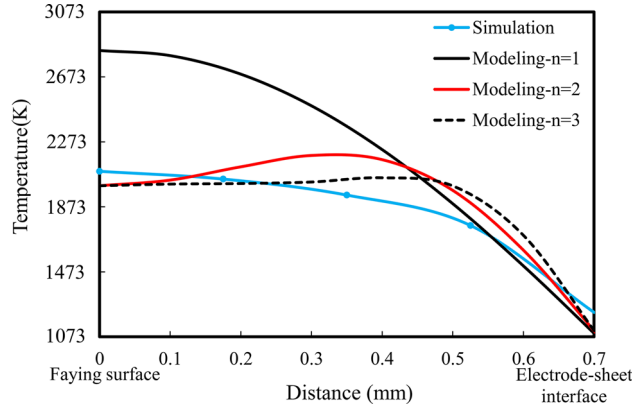| β Value	Numerically Predicted T_{max} K (°C)	Analytically Predicted T_{max} K (°C)		
		$n = 1$	$n = 2$	$n = 3$
0.75 (12 kA)	2073 (1800)	2833 (2560)	2013 (1740)	2013 (1740)
0.6 (10 kA)	1923 (1650)	2043 (1770)	1843 (1570)	1825 (1552)
0.3 (8 kA)	1803 (1530)	1837 (1564)	1797 (1524)	1797 (1524)

Fig. 7—Predicted temperature profile along the sheet thickness by the analytical and numerical models for the welds created by 12-kA welding current.

V. DISCUSSION

To calculate the temperature distribution and the cooling rate, some basic information is required, including β, T_S, and T_{max}. β can be determined by experimental measurements. T_{max} and T_S can also be calculated by introducing Eq. [9] into Eq. [7] and setting the nugget boundary temperature equal to the liquidus temperature in the resultant equation; *i.e.*, $T(z_{FL}) = T_l$.

The accuracy of the T_{max} predicted by the analytical method depends on n and β. In Table III, the effects of n on T_{max} are given at three different β values. It can be observed that at higher nugget penetrations (β), to reach more accurate results, the selection of the larger values for n seems necessary. The effect of n on the accuracy of the analytical model to predict the temperature profile at $\beta = 0.75$ is shown in Figure 7. Evidently, $n = 3$ led to more accurate results and T_{max} was overestimated when $n = 1$.

In the analytical model, not only T_{max} but also the calculated cooling rates were dependent on n. Figure 8 illustrates numerically and analytically computed cooling rates at three different zones, *i.e.*, nugget zone (z, $r = 0$), lateral HAZ ($z = 0$ and $r > r_{FL}$), and axial HAZ ($z > z_{FL}$ and $r = 0$).

In this figure, the variations of the cooling rates are plotted against temperature during the cooling step for the welded sample using 10-kA welding current. It should be mentioned that the differences between the obtained results at $n > 3$ and $n = 3$ are insignificant even at high nugget penetrations (β). Therefore, in this investigation, the calculations were limited to $n = 1, 2,$ and 3.

The results of the calculation corresponding to the nugget center (z, $r = 0$) are depicted in Figure 8(a). Regarding the simulation results, because of the released latent heat, the cooling rate was reasonably low during the solidification process; at the end of solidification, it suddenly increased. Neglecting this latent heat in the analytical model leads to uncertain results in the solidification temperature range. However, the reliability of the analytical model at higher temperatures can be improved if larger values are selected for n.

The comparison between the analytically and numerically predicted cooling rates for a point located at the axial HAZ ($z > z_{FL}, r = 0$) is also shown in Figure 8(b). As shown in this figure, two models were consistent with each other especially at larger n. Besides, the present model could accurately predict the peak temperature of the HAZ (the HAZ temperature at the current termination instance). The temperature history of the lateral HAZ could also be estimated by the analytical model. Indeed, simulation results demonstrated that, at the beginning of the cooling step, the overall shape of the temperature profile at $r > r_{FL}$ was close to $r = 0$ (Figure 7). Thus, this profile could be used for the lateral HAZ. Nonetheless, it is mandatory to note that, for the lateral HAZ ($r > r_{FL}$), T_{max} in Eqs. [5] and [7] should be replaced by the peak temperature of the studied point. Figure 8(c) illustrates the cooling rate variations for a point located at the lateral HAZ, where 1393 K (1120 °C) was the peak temperature experienced by this point. It can be seen that, at the beginning of the cooling step, with decreasing the temperature, the cooling rate increased to a maximum value, and then, with further temperature reduction, the cooling rate reduced again.

The differences between the cooling rates at the lateral and axial HAZs can be explained using the initial temperature distribution along the sheet thickness. In line with Eq. [2], it is generally accepted that the cooling rate is roughly proportional to the temperature profile curvature. Regarding Figure 7, at the axial HAZ (near the electrode-sheet interface), the initial temperature distribution had a higher curvature compared with that at the faying surface ($z = 0$). Thus, immediately after the current termination, the axial HAZ experienced high cooling rates. With the rapid temperature reduction in the axial HAZ, the curvature of the temperature profile began to increase at the faying surface and, in turn, the cooling rate raised at this zone. Thereafter, with greater temperature reduction at the faying surface, the corresponding curvature reduced and, subsequently, the cooling rate decreased again.
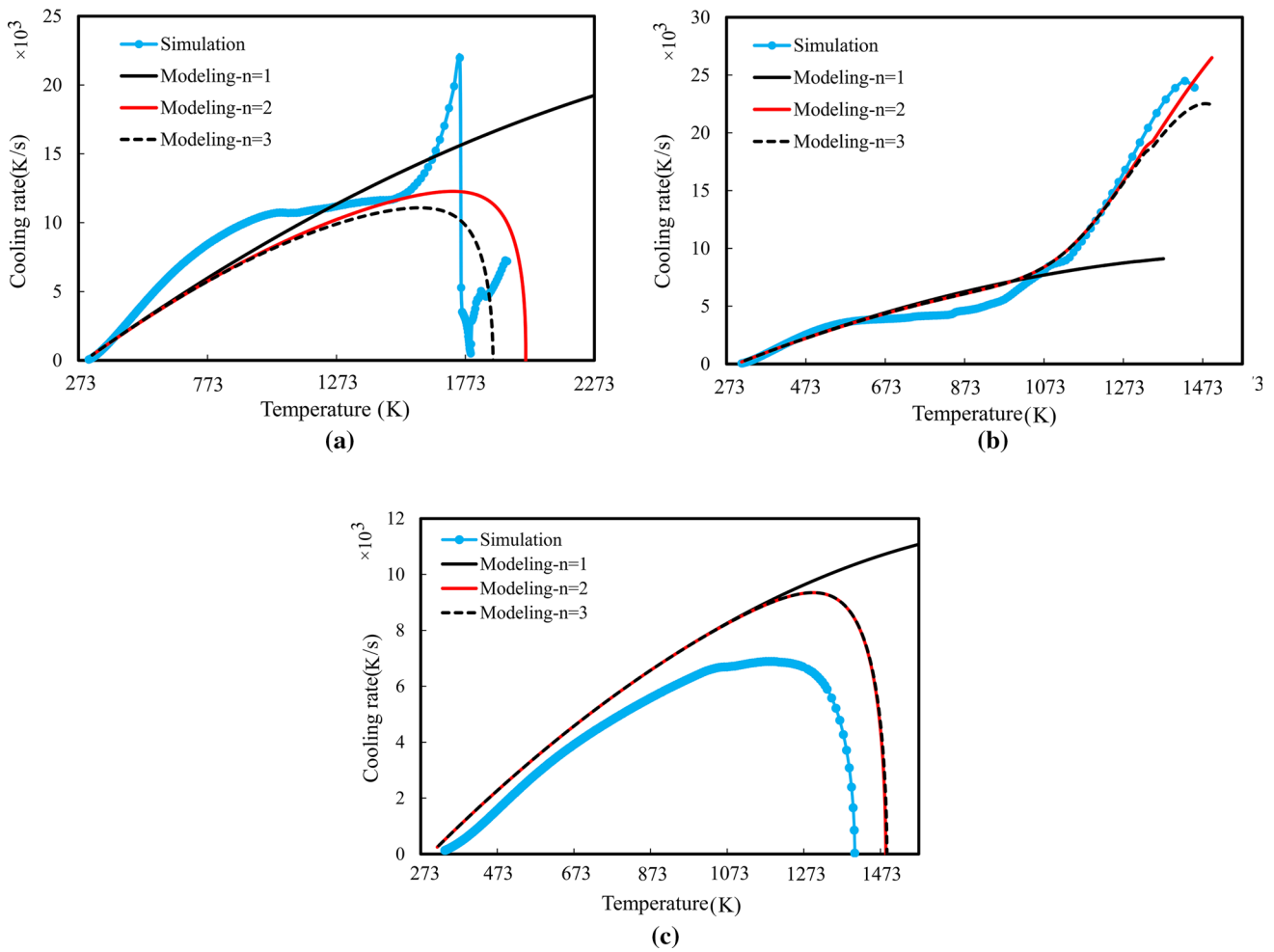
Fig. 8—Cooling rate computed as a function of temperature by the analytical (at different values of n) and numerical models during the cooling step at different locations of the weld zone performed by 10 kA: (a) $z, r = 0$; (b) $z = 0.75 \times h$, $r = 0$; and (c) $z = 0$, $r > r_{FL}$, $T_{max,r} = 1393$ K (1120 °C).
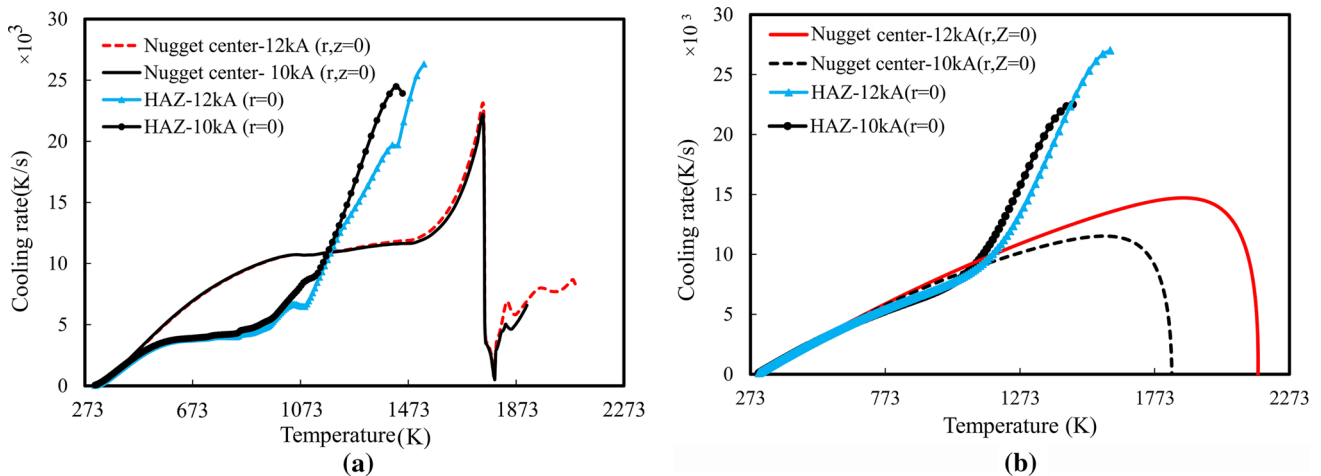

Fig. 9—Variation of the cooling rates as a function of temperature corresponding to the nugget center ($r, z = 0$) and axial HAZ at two different welding currents predicted by the (a) numerical and (b) analytical models.

Dependency of the analytical results on n, especially at temperatures above $T_1/2$, was obvious in all the discussed figures. It is interesting to note that, in lower temperature ranges ($T < T_1/2$), the results did not have any dependency on n. In other words, to study the phase transformations at temperatures below $T_1/2$, choosing
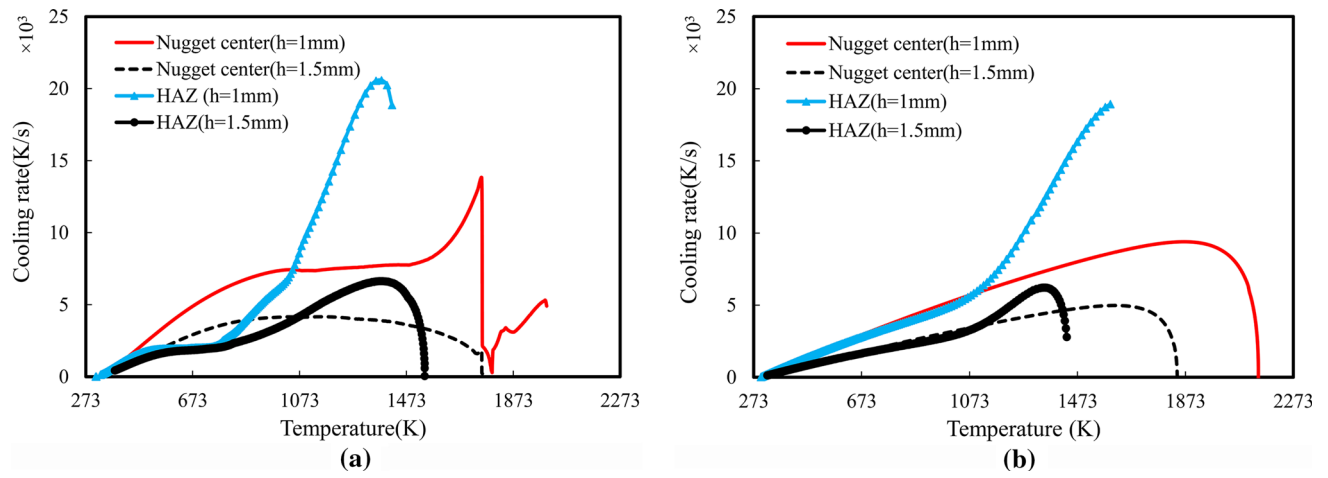
Fig. 10—Reducing the cooling rate in the nugget center and axial HAZ by increasing the sheet thickness: (a) numerical model and (b) analytical model.
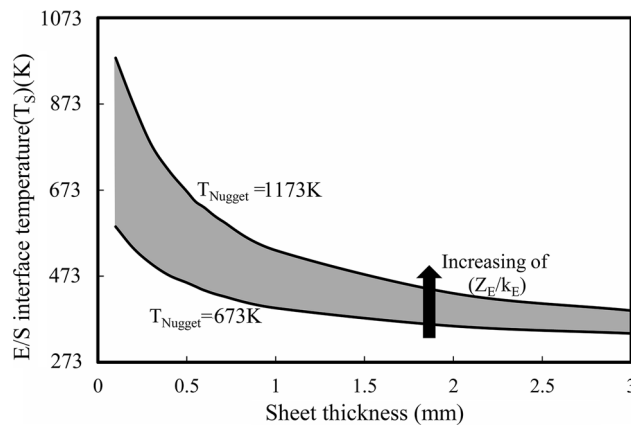

Fig. 11—Variation range of E/S temperature (T_S) during the decomposition of the nugget from austenite to other phases as a function of sheet thickness. An increase in Z_E/k_E leads to an increase in the upper and lower boundaries of T_S variations.
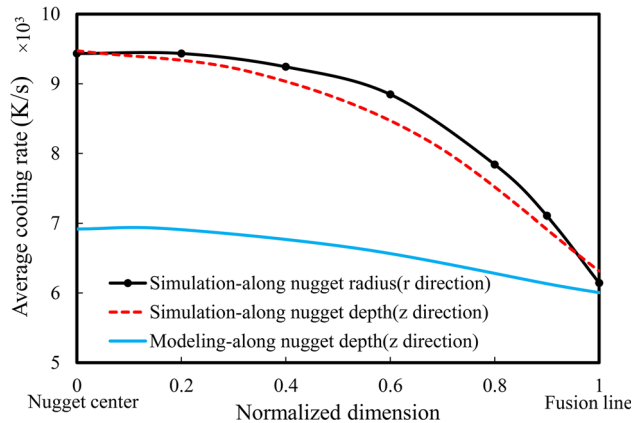

Fig. 12—Variation of the average cooling rate during austenite decomposition [i.e., between 1173 K and 673 K (900 °C and 400 °C)] as a function of the normalized nugget dimensions.

larger values for n is not necessary and the assumption $n = 1$ can lead to reliable results. Consequently, for low-temperature transformation, cooling rates can be obtained by differentiating Eq. [7] with respect to time as follows:

$$\dot{T} = \frac{\alpha \pi^2}{4h^2}(T - T_S), \qquad [10]$$

Regarding this equation, the cooling rate at any temperature is mainly affected by the sheet thickness and T_S. Any reduction in the sheet thickness and T_S can result in a higher cooling rate.

VI. EFFECTS OF WELDING CURRENT AND SHEET THICKNESS

Figure 9 shows the effects of welding current on the cooling rate of the nugget and HAZ in the resistance welding of 0.7-mm-thick steel sheets.

The analytical results shown in this figure are plotted based on $n = 3$. It can be seen that both models confirmed that the experienced cooling rates by the nugget center and axial HAZ were not significantly affected by welding current (10 and 12 kA) and, in turn, T_{max}. Indeed, higher welding currents only increased the dimensions of the nugget zone and the HAZ.

Regarding Eq. [10], the sheet thickness can be a critical factor governing the cooling rate in RSW. The validity of this result was evaluated by the numerical simulations. The computational studies were conducted on the welding of 1- and 1.5-mm-thick sheets at similar nugget penetrations ($\beta = 0.5$). The results indicated that as the steel sheets thickened more, the nugget zone and HAZ experienced lower cooling rates; the obtained results corresponding to both models are shown in Figure 10.

Nevertheless, it is interesting to note that, based on Eq. [9], the sheet thickness can also affect the T_S. Decomposition of austenite is one of the most important transformations in steels that should be considered as low-temperature transformation. Figure 11 illustrates the variation range of T_S during this phase
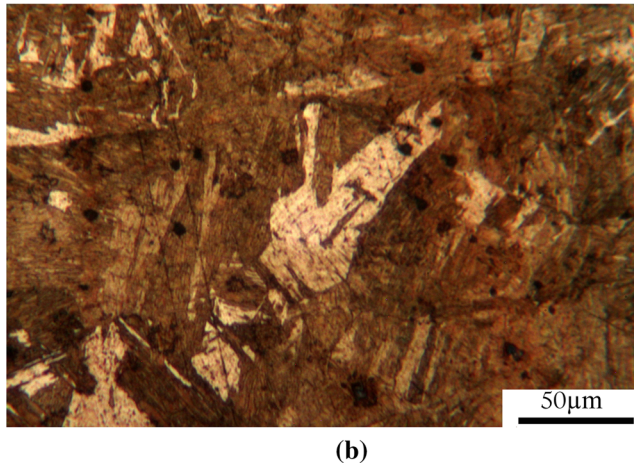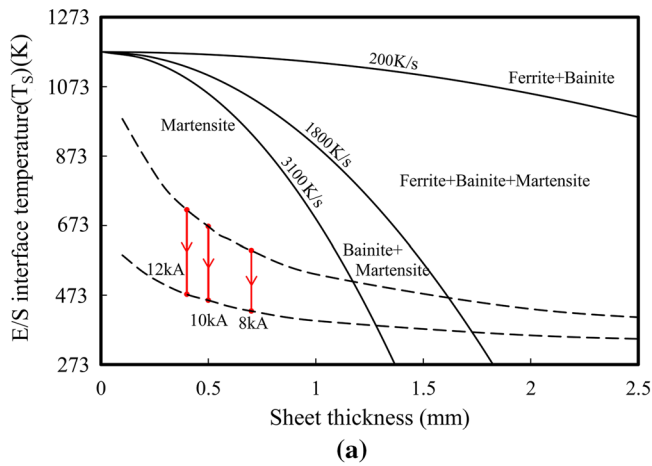
Fig. 13—Microstructural aspects. (*a*) The microstructure map established against the sheet thickness and the electrode-sheet interface temperature (T_S) for the studied material. The red arrows on this map show the T_S variations at the instance of the nugget phase transformation considering joint thickness at different welding conditions. (*b*) The martensitic microstructure of the nugget zone formed at 10-kA welding current.

transformation as a function of sheet thickness obtained from the analytical model (gray zone in this figure).

It can be observed that, with increasing the sheet thickness, T_S decreases. Moreover, a larger ratio of Z_E to k_E leads to a higher temperature at the sheet-electrode interface.

The variations of the average cooling rate during austenitic nugget decomposition [temperatures between 1173 K and 673 K (900 °C and 400 °C)] are given in Figure 12.

These calculations were performed for different points along the z and r directions in the nugget. In this figure, these variations are shown against normalized dimensions; 0 and 1 represent the nugget center and boundary, respectively. It can be seen that, with getting close to the nugget center, the average cooling rate along both paths slightly increased with the same trend. These differences in the average cooling rate at various points were attributed to the continuous reduction of T_s during nugget cooling. Indeed, at locations close to the nugget boundary, in comparison with the nugget center, austenite decomposition took place faster, *i.e.*, when T_s was higher. Therefore, with regard to Eq. [10], the average cooling rate at the nugget boundary was lower and increased with getting closing to the nugget center.

Equation [11] relates the hardness of martensite to the cooling rate and steel composition.[2] Based on this equation, this range of variations in the cooling rates could not have noticeable effects on the hardness of martensite.

$$Hv_M = 127 + 949C + 27Si + 11Mn + 8Ni + 16Cr + 21\log \dot{T},$$
[11]

where $\dot{T}$ is the cooling rate (Kelvin per hour) at 973 K (700 °C) and the element symbols refer to their content in weight percent. This claim can also be confirmed by the relatively consistent hardness of the nugget zone, as shown in Figure 4(a), and the results reported in other investigations.[1,2,16–18] Besides, it can also be inferred

that, although this model is one dimensional, it can be used for the entire nugget zone since different points located along the z and r directions, in the same normalized distance from the nugget center, follow the same thermal cycle.

Figure 12 reveals that the maximum difference between the average cooling rates predicted by the numerical and analytical models did not exceed 20 pct; these differences can be attributed to the input data of the model. In contrast to the numerical simulations, where the temperature dependency of input parameters was taken into account, for the analytical model, the average values between solidus and room temperatures were considered for calculations.

The final microstructure of the nugget can be determined by the estimation of the cooling rate at the instance of austenite decomposition using Eq. [10]. Figure 13(a) exhibits a microstructure map, plotted for the studied steel, as a function of the sheet thickness and T_S. The boundaries in this figure are plotted based on the cooling rates in which the resultant microstructure will be changed when austenite is cooled from the upper critical temperature, *i.e.*, A_3, or 1173 K (900 °C). These cooling rates can be derived from CCT diagrams. The variations of T_S with the sheet thickness are also depicted by dashed lines in this figure. Thus, knowing the sheet thickness at the welding zone, one can easily predict the nugget microstructure using this map.

Figure 13(a) shows that, as the cooling rate increased, the corresponding curve moved to the left. Therefore, increasing the critical cooling rate could reasonably incline the martensite region boundary to the left; as expected, the corresponding area in the map decreased. For all conditions, the cooling rate was high enough to produce a martensitic microstructure in the nugget.

The higher nugget hardness at higher welding currents can be justified using the present analytical model and Eq. [11]. The predicted hardnesses of the nuggets based on the analytical results at 8-, 10-, and 12-kA welding currents were 296, 320, and 324 Hv, respectively. Indeed, as the welding current increases, the joint

thickness decreases and, in turn, the hardness of the nugget increases. It was observed that the calculations of this study were in relatively good agreement with the experimental measurements reported in Figure 4.

VII. CONCLUSIONS

In summary, a one-dimensional analytical model (*n*-term series) was established to predict the thermal history along the sheet thickness in RSW. This model could calculate the cooling rate with relatively good accuracy. The accuracy of the proposed model at high temperatures ($T > T_l/2$) depended on *n*; to avoid excessive error, in these cases, *n* should be larger than 2. For low-temperature transformations, such as austenite decomposition, $n = 1$ led to reliable results. It was demonstrated that this model could accurately be applied to predict the cooling rate in both lateral and axial HAZs. For low-temperature transformations ($T < T_l/2$), among all process parameters, the joint thickness and the temperature of the electrode-sheet interface were the most important factors governing the cooling rate. A simple approach was put forward to plot a quantitative microstructural map for steels based on the proposed analytical model.

ACKNOWLEDGMENTS

REFERENCES

1. H. Zhang and J. Senkara: *Resistance Welding: Fundamentals and Applications*, CRC Press, London, 2005, pp. 1–17.
2. M. Pouranvari and S.P.H. Marashi: *Sci. Technol. Weld. Join.*, 2013, vol. 18, pp. 361–403.
3. Z. Han, J.E. Indacochea, C.H. Chen, and S. Bhat: *Weld. J.*, 1993, vol. 72, pp. 209s–16s.
4. J.E. Gould: *Weld. J.*, 1987, vol. 66, pp. 1s–11s.
5. A. Joaquin, A.N.A. Elliott, and C. Jiang: *Weld. J.*, 2007, vol. 86, pp. 24–27.
6. H. Eisazadeh, M. Hamedi, and A. Halvaee: *Mater. Des.*, 2010, vol. 31, pp. 149–57.
7. N.T. Williams and J.D. Parker: *Int. Mater. Rev.*, 2004, vol. 49, pp. 45–75.
8. X. Wan, Y. Wang, and P. Zhang: *J. Mater. Process. Technol.*, 2014, vol. 214, pp. 2723–29.
9. C.L. Tsai, O.A. Jammal, and D.W. Dickinson: *Weld. J.*, 1992, vol. 71, pp. 47s–54s.
10. J.A. Khan, L. Xu, and Y.-J. Chao: *Sci. Technol. Weld. Join.*, 1999, vol. 4, pp. 201–07.
11. D. Richard, M. Fafard, R. Lacroix, P. Clery, and Y. Maltais: *J. Mater. Process. Technol.*, 2003, vol. 132, pp. 119–31.
12. E. Feulvarch, V. Robin, and J.M. Bergheau: *J. Mater. Process. Technol.*, 2004, vol. 153, pp. 436–41.
13. M. Eshraghi, M.A. Tschopp, M.A. Zaeem, and S.D. Felicelli: *Mater. Des.*, 2014, vol. 56, pp. 387–97.
14. J.E. Gould, S.P. Khurana, and T. Li: *Weld. J.*, 2006, vol. 85, pp. 111s–16s.
15. H. Zhigang, W. Yuanxun, L. Chunzhi, and C. Chuanyao: *Acta Mech. Solida Sin.*, 2006, vol. 19, pp. 86–94.
16. W.L. Chuko and J.E. Gould: *Weld. J.*, 2002, vol. 81, pp. 1s–7s.
17. M.I. Khan, M.L. Kuntz, E. Biro, and Y. Zhou: *Metall. Mater. Trans. A*, 2008, vol. 49A, pp. 1629–37.
18. Y.S. Jong, Y.K. Lee, D.C. Kim, M.J. Kang, I.S. Hwang, and W.B. Lee: *Metall. Mater. Trans. A*, 2011, vol. 52A, pp. 1330–33.